Carbon Ion Implantation Effects on Morphology, Bandgap, and Urbach Tailing in ZnO Thin Films

K. SUCHANEK a,* , K. Wojtasik a , O. Łoś a , M. Mitura-Nowak b and S. Kąc c

^a Cracow University of Technology, Faculty of Materials Engineering and Physics, Department of Physics, Podchorążych 1, 30-084 Kraków, Poland

^bInstitute of Nuclear Physics, Polish Academy of Sciences, Radzikowskiego 152, 31-342 Kraków, Poland

^cAGH University of Science and Technology, Department of Surface Engineering and Materials Characterisation, Faculty of Metals Engineering and Industrial Computer Science, al. A. Mickiewicza 30, 30-059 Kraków, Poland

Received: 30.05.2025 & Accepted: 01.09.2025

Doi: 10.12693/APhysPolA.148.89 *e-mail: katarzyna.suchanek@pk.edu.pl

Zinc oxide (ZnO) is a wide-bandgap semiconductor with diverse applications in optoelectronics and sensing. In this study, we examine how 20 keV C⁺ ion implantation affects the morphology and optical properties of ZnO thin films. Using atomic force microscopy and ultraviolet-visible spectroscopy, we observe that ion implantation leads to a reduction in grain size, increased morphological disorder, and a fluence-dependent increase in both the optical bandgap and Urbach energy. Simulations using the Transport of Ions in Matter code indicate that implanted ions penetrate the ZnO layer to an average depth of around 41 nm, generating near-surface structural damage. Post-implantation annealing at 500°C partially restores the optical properties, indicating some level of defect recovery. These findings demonstrate that low-energy carbon ion implantation enables controlled tuning of the properties of ZnO thin film without structural degradation.

topics: ion irradiation, zinc oxide, thin films, ultraviolet-visible (UV-Vis) spectroscopy

1. Introduction

Zinc oxide (ZnO) is a wide-bandgap semiconductor from II–VI group that is recognized for its large exciton binding energy ($\sim 60 \text{ meV}$), high transparency in the visible range, and strong ultraviolet (UV) absorption [1, 2]. With a bandgap of 3.37 eV at room temperature, high carrier mobility (up to $\sim 400 \text{ cm}^2/(\text{V s})$) and excellent chemical stability, ZnO is widely investigated for optoelectronic and sensing applications, including light-emitting diodes (LEDs) [3, 4], photodetectors [5, 6], solar cells [7], and gas sensors [8–10]. Additionally, it plays a key role in photochemical water splitting [11], catalysis [12, 13], biomedical technologies [14, 15] and active food packaging [16, 17]. Its abundance, costeffective synthesis and simple fabrication methods sustain strong interest in both fundamental research and practical applications [1]. However, despite its versatile properties, precise control over the defect states, surface chemistry, and doping of ZnO remains essential for tailoring its electronic and optical behavior in advanced applications.

Ion implantation is a widely used technique for modifying the properties of materials, including ZnO [18]. During this process, high-energy ions penetrate the material, losing energy through inelastic and elastic collisions. In the former process, energy is transferred to the electronic system of the material, leading to its excitation or ionization. In contrast, elastic collisions result in direct transfer of the energy to target atoms, causing the formation of point defects, structural reorganization, and morphological changes [18–20]. The introduction of the defects into the ZnO crystal lattice through ion implantation significantly affects its optoelectronic properties. Among the potential defects, oxygen vacancies (V_O) and zinc interstitials (Zn_i) can act as deep-level traps, altering carrier dynamics and recombination rates [21, 22]. Oxygen vacancies often introduce localized energy states within the bandgap, leading to enhanced light absorption and improved photocatalytic activity. For instance, research has demonstrated that an increase in oxygen vacancies results in a narrowing of the bandgap, thereby increasing visible light absorption in ZnO [23]. Additionally, oxygen vacancies can induce carrier localization, which improves charge separation and contributes to improved photocatalytic performance [24].

ZnO single crystals are known for their radiation tolerance. Numerous investigations have shown that ZnO does not undergo amorphization, even at high ion fluences and displacement levels [25–27]. Kucheyev et al. [25] conducted a detailed analysis of defect formation in ZnO implanted with $\mathrm{Au^{+}}$ and $\mathrm{Si^{+}}$ ions at room temperature and 77 K, revealing the dynamic annealing effects. Notably, even at high fluences of heavy Au⁺ ions, no evidence of amorphization was observed. Similarly, Lorenz et al. [26] investigated the effects of N^+ , Ar⁺ and Er⁺ ion implantation in ZnO at low temperature. Although they identified several stages of damage accumulation and defect evolution, the material retained its crystalline structure across the fluence range studied. Chen et al. [27], who compared the defect recovery behaviour of ZnO implanted with B⁺ and O⁺ ions, demonstrated that the annealing behavior strongly depends on the ion species. Despite growing interest in ion-beamassisted tuning of ZnO properties, carbon ion implantation remains relatively unexplored. Carbon is a nonmetallic dopant. First-principles density functional theory (DFT) calculations by Sharma et al. [28] revealed that although the carbon-induced impurity bands do not significantly narrow the bandgap, they introduce localized states near the band edges, enhancing absorption in the visible range. Experimental studies of C-implanted ZnO films have shown that at low concentrations, interstitial carbon induces ferromagnetism via charge transfer between O-2p states and defect levels, while at higher concentrations, substitutional C and Zn vacancies become dominant. High-fluence samples retained their magnetic response even after annealing at 500°C [29]. Similarly, Zhou et al. [30] demonstrated that C-implanted ZnO exhibits room temperature ferromagnetism with a Curie temperature above 300 K. While the experimental studies [29, 30] focused on magnetic properties, the present work focuses on the effects of 20 keV C⁺ ion implantation on nanostructured ZnO thin films, with particular attention to surface restructuring and defect-mediated optical modifications. The structural evolution is examined before and after postimplantation annealing, while the Urbach energy is used as a quantitative probe of the sub-bandgap absorption linked to disorder-induced localized states.

2. Materials and methods

2.1. Materials

Zinc acetate dihydrate $(Zn(CH_3COO)_2 \cdot 2H_2O)$ and diethanolamine $(C_4H_{11}NO_2)$ were purchased from Chempur (Poland). Tetrapropenyl

succinic anhydride (TPSA) was purchased from BASF Polska (Poland) and 99.8% ethanol was used from Avantor (Poland). Deionized water was used directly from a deionizer (Polwater DL2-100S613TUV, Labopol Solutions & Technologies, Kraków, Poland). Soda-lime microscope glasses (Menzel Gläser, Thermo Scientific, Waltham, USA) were used as substrates. All chemicals were of analytical reagent grade.

2.2. Preparation of ZnO thin films

The sol was prepared as follows. A solution of 6 mmol of zinc acetate dihydrate in ethanol (10 ml) was thoroughly stirred at 50°C for 30 min. Then, 3 mmol of diethanolamine as a stabilizer and 10 mmol of deionized water were added dropwise until the solution became transparent. The mixture was then magnetically stirred at 50°C for 2 h, and the resulting sol was left to age for another 30 days before the deposition process [31]. A clear, colorless sol was obtained. Thin ZnO thin films were produced by spin-coating. Glass substrates of dimensions $25 \times 25 \times 1$ mm³, before sol application, were mechanically cleaned with water and detergent, rinsed with deionized water, isopropyl alcohol, diluted acetic acid and acetone. Deposition was carried out at a speed of 2000 rpm for 30 s. Finally, the ZnO thin films were annealed under oxidizing conditions in a furnace at 485°C for 60 min. The resulting film thickness, as determined by spectroscopic ellipsometry, was approximately 95 nm.

2.3. Carbon ion implantation schemes

ZnO thin films were implanted with C⁺ carbon ions using a dedicated ion implanter, described in detail in [32]. The acceleration energy was set to 20 keV, and the typical ion beam current density was 1 μ A/cm². The pressure inside the implantation chamber was maintained at 1 × 10⁻⁶ Pa. Implantation was conducted at room temperature, with the ion beam incident perpendicular to the sample surface. The samples were mounted on a movable sample holder, which enabled uniform irradiation across the entire film surface. Three different C⁺ ion fluences (Φ) were selected: 1 × 10¹⁴, 1 × 10¹⁵, 1 × 10¹⁶ ions/cm².

2.4. Optical and morphological characterization

The morphology of the synthesized coatings was examined using a Dimension \mathbb{R} Icon \mathbb{R} Scanning Probe Microscope (SPM) manufactured by Veeco Instruments Inc., operated as an atomic force microscope (AFM) with the ScanAsyst in air mode.

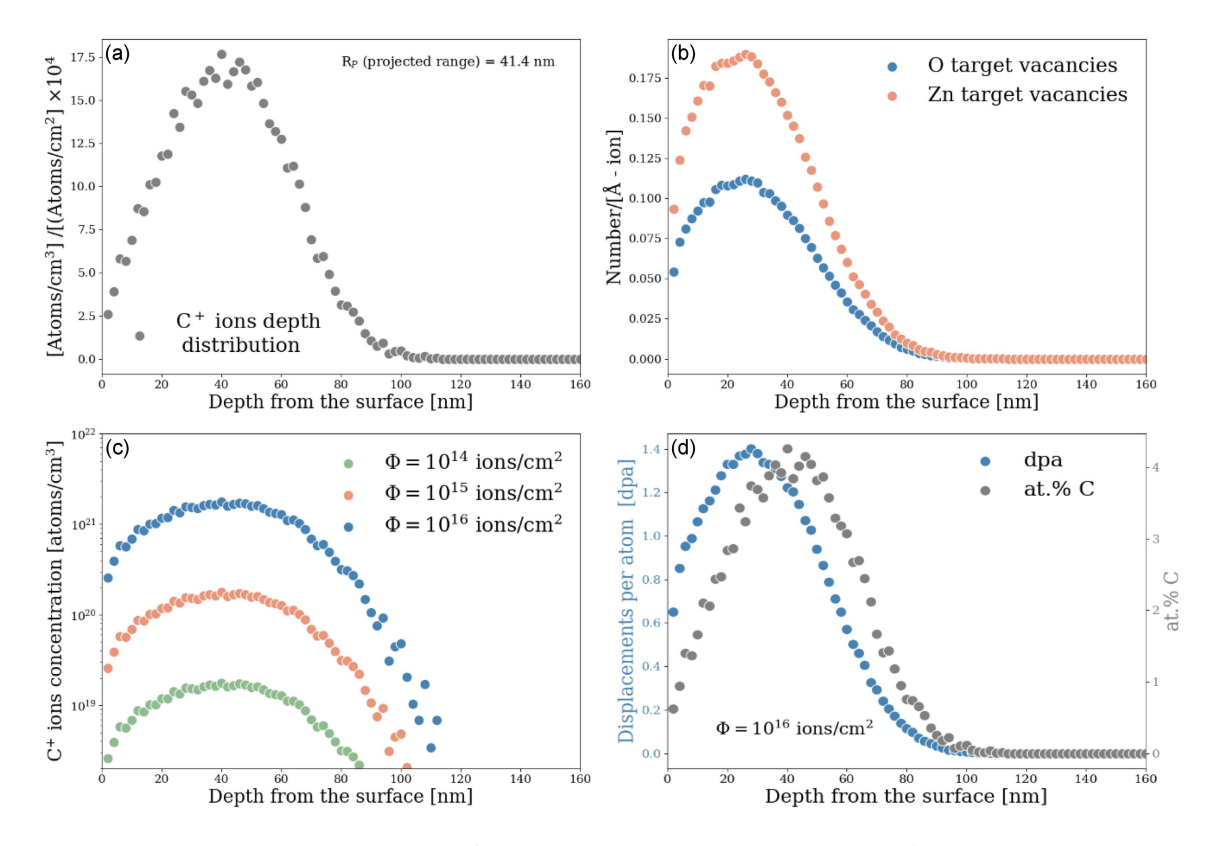


Fig. 1. TRIM calculations for 20 keV C^+ implantation in ZnO thin films. (a) C^+ ion ranges. (b) Zn (V_{Zn}) and O (V_O) vacancy depth profiles. (c) Carbon ions concentration profiles for three different fluences. (d) Displacements per atom (dpa) and atomic% C vs depth.

ScanAsyst is based on Veeco's patented, Peak Force Tapping™mode. This allows to operate at even lower forces than traditional tapping mode, which helps protect delicate samples and tips. The obtained surface topography images were processed using Bruker's NanoScope Analysis 2.0 software.

Transmittance and reflectance characteristics of the thin films were recorded using a Lambda 900 UV/VIS/NIR Spectrophotometer (Perkin Elmer) equipped with an integrating sphere. Measurements were performed in the 200–800 nm range at room temperature.

3. Results and discussion

3.1. SRIM and TRIM calculations

To better understand the interactions of a carbon ion with a thin ZnO layer, we first performed numerical calculations of the implantation process using the TRIM (Transport of Ions in Matter) code, which is a part of the SRIM (Stopping and Range of Ions in Matter) package. This tool is widely used to model the interaction of energetic ions with solids. TRIM employs a Monte Carlo approach based on the binary collision approximation to simulate collision cascades and calculate

parameters such as the projected range of implanted ions, energy loss, and distribution of displacements in the target material [33]. Through numerical calculations, we gained insights into the extent and nature of damage formation. We performed TRIM simulations in detailed full-damage cascade mode to investigate defects induced by C⁺ ion bombardment on a thin ZnO layer. The displacement threshold energy (E_d) was set to 44 eV for oxygen and 34 eV for zinc [34]. The displacement threshold energy defines the minimum kinetic energy required for an atom in a crystalline lattice to be permanently displaced from its site, leading to the formation of a vacancy or defect. If the collision energy is below E_d , the atom is merely displaced but returns to its original position without creating a vacancy.

Figure 1a illustrates the depth distribution of 20 keV C⁺ ions in a ZnO layer. The bulk ZnO density of 5.61 g/cm³ was used in the calculations. The figure shows that the ion distribution in the layer follows a Gaussian profile, and the ions are retained in a thin layer near the surface, reaching a depth of 100 nm. The projected range, representing the average depth to which an ion penetrates the target before being retained, was determined to be 41.4 nm. The implantation energy of 20 keV was selected to ensure that the implanted ions remain fully within the ZnO layer, the thickness of which was determined by spectroscopic ellipsometry

to be ≈ 95 nm. During implantation, a number of processes occur, i.e., the incident C⁺ ion interacts with the atomic system of the layer and, as a result of nuclear (elastic) and electronic (inelastic) scattering, changes its direction and loses its velocity. In this process, the lattice atoms are displaced from their original positions due to collisions, and various types of lattice defects, such as point defects and vacancies, are formed. Figure 1b shows the distribution of ion-induced Zn vacancies $(V_{\rm Zn})$ and O vacancies (V_O) in the crystal lattice. We can see that the introduction of carbon ions causes a significant number of vacancy defects extending to a depth of about 100 nm from the material surface. Simulations show that $\rm V_{\rm Zn}$ vacancies are generated more efficiently than $\rm V_{\rm O}$ vacancies, which is consistent with the lower displacement energy (E_d) for Zn atoms. Figure 1c shows the profile of C⁺ ion concentration [in atoms/cm³] as a function of depth from the sample surface, for three different ion fluences during ion implantation. For all fluences, the maximum concentration is located at a small depth from the surface (around 30–50 nm).

In order to calculate the atomic implantation ion concentration [in at.%] and the fluence-dependent total vacancy concentration, i.e., $(V_{Zn} + V_O)$ displacement damage^{†1} from SRIM output files, we used the following equations, respectively [35]

carbon ion concentration [at.% ion] =

ion distribution per unit fluence $\left[\frac{\text{atoms/cm}^3}{\text{atoms/cm}^2}\right]$

$$\times \left(\frac{\mathrm{fluence\ [ions/cm^2]}}{5.61 \times 10^{22}\ \mathrm{atoms/cm^3}}\right) \times 100 = \\ \left[\frac{\mathrm{ions}}{\mathrm{atom}}\right] \times 100$$

and

displacement damage (dpa) =

$$\frac{\text{vacancies}}{\text{ions} \times 1 \text{ Å}} \frac{10^8 \text{ Å/cm} \times \text{fluence } \left[\text{ions/cm}^2\right]}{5.61 \times 10^{22} \text{ atoms/cm}^3} = \frac{\text{number of vacancies}}{\text{atom}}.$$
(2)

The results for the highest ion fluence $(\Phi=10^{16}~{\rm ions/cm^2})$ are presented in Fig. 1d. Maximum damage to the crystal lattice as a result of collisions of ions with material atoms occurs at a depth of about 30–35 nm. The atomic carbon content, i.e., the number of carbon atoms expressed as a percentage of all atoms in a given area, has a maximum value of $\simeq 4$ at.% C at a slightly greater

depth, about 50–55 nm. As a result of implantation, C^+ ions interact with the ZnO crystal lattice, and the collisions with the target atoms occur close to the surface. In this region, the ions have the highest energy, causing damage in the lattice (e.g. vacancies, interstitial atoms). Deeper into the material, due to the slowing-down process, the ions lose energy through interactions with electrons and subsequent collisions with lattice atoms, and the energy drops below the threshold E_d . However, the C^+ ions continue to move deeper into the material and we see that the maximum damage (dpa) occurs shallower than the maximum carbon concentration (at.% C).

3.2. Morphology of ZnO thin films before and after implantation

The topographic properties of ZnO thin films before and after implantation were studied using atomic force microscopy. Figure 2 shows 2D and 3D images obtained from a scanned area of $1 \times 1 \ \mu \text{m}^2$ of the control sample (Fig. 2a-b) as well as samples implanted with three different fluence of C⁺ ions (Fig. 2c-h). AFM images reveal a granular morphology with well-defined, rounded nanostructures distributed across the surface. The size of the granular structures appears relatively uniform, with individual features exhibiting a spherical shape and size in the range of \approx 70–100 nm for the nonimplanted sample (Fig. 2a-b), and 40-70 nm for all applied ion fluences (Fig. 2c-h). Notably, the ZnO surface implanted with C⁺ demonstrates granular structures that are more uniform in shape and reduced in size compared to the non-implanted counterpart. However, the size distribution of the granular morphology appears broader, with a significant presence of both smaller and larger structures. This suggests that ion implantation induces a redistribution of material at the nanoscale, leading to a more heterogeneous structure. This modification can be attributed to ion-beam-induced recrystallization processes and the associated morphological evolution of the surface. Importantly, the ZnO layer implanted with the highest ion fluence (i.e., $1 \times 10^{16} \text{ ions/cm}^2$) remained structurally intact, with no evidence of morphological degradation or loss of continuity. However, the absence of morphological deterioration does not necessarily imply that the material retains its original crystallinity. Considering the estimated carbon concentration of $\approx 10^{21} \text{ cm}^{-3}$ in the implanted thin layer, the possibility of implantation-induced structural disorder, as well as significant alterations in the local crystallographic arrangement, cannot be excluded.

Based on the AMF results, surface roughness parameters were quantified, including the root mean square roughness R_q , the maximum roughness R_{\max} , the average roughness R_a . The parameter R_a

(1)

^{†1}Displacements per atom (dpa), i.e., the number of vacancies produced per atom, quantifies the amount of damage to the crystal lattice as a result of collisions of ions with the atom of the material.

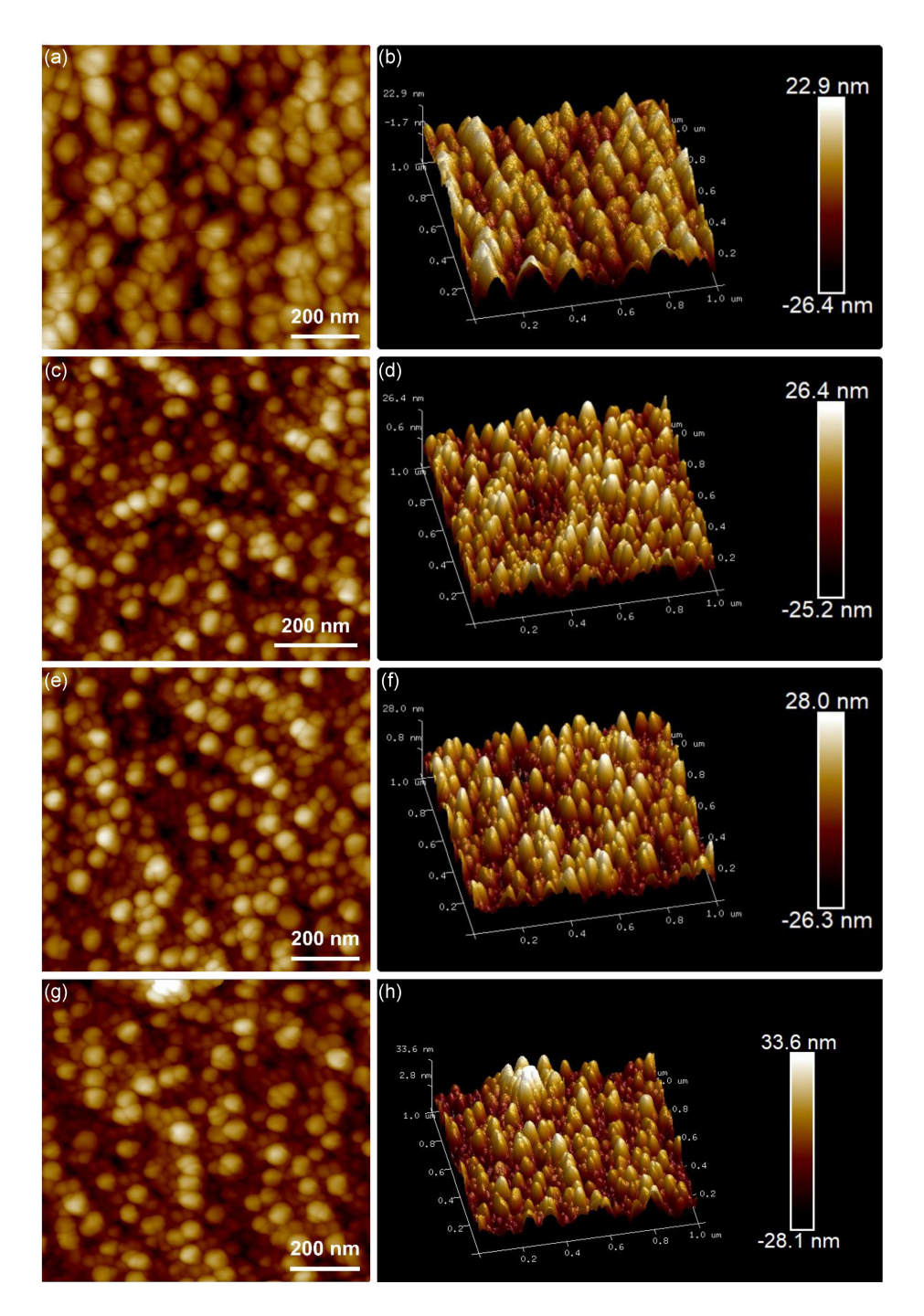


Fig. 2. 2D and 3D AFM images of ZnO thin film. (a, b) Surface of the control sample prior implantation. (c-h) Surface of samples implanted with 20 keV C⁺ ions at different fluences: (c, d) $\Phi = 10^{14}$ ions/cm², (e, f) $\Phi = 10^{15}$ ions/cm², (g, h) $\Phi = 10^{16}$ ions/cm².

denotes the arithmetic average of the absolute deviation of the surface height from the plane, while $R_{\rm max}$ represents the maximum vertical distance between the highest and lowest points in the topographic profile. The obtained results are summarized in Table I. The findings indicate substantial modifications in surface roughness induced by energetic ion bombardment. For the control sample, the measured roughness parameters were $R_a = 5.80$ nm, $R_q = 7.20$ nm,

and $R_{\rm max}=43.2$ nm. During ion implantation, a progressive increase in roughness was observed with increasing fluence, reaching $R_a=7.27$ nm, $R_q=9.11$ nm, and $R_{\rm max}=75.0$ nm at the highest fluence (i.e., $1\times 10^{16}~{\rm ions/cm^2}$). This increase is attributed to the interaction of energetic C⁺ ions with the ZnO lattice, leading to the formation of structural defects, localized atomic displacements, and surface reorganization that alter the surface. These structural modifications contribute to the

TABLE I Surface roughness parameters $(R_q, R_a, R_{\text{max}})$ of ZnO thin films determined from AFM measurements.

Fluence	R_q [nm]	R_a	$R_{\rm max}$
	[nm]	[nm]	[nm]
Control (before implantation)	7.20	5.80	43.2
$arPhi_1=10^{14}~{ m ions/cm^2}$	8.29	6.72	50.5
$\Phi_2=10^{15}~\mathrm{ions/cm}^2$	8.06	6.54	50.2
$\Phi_3 = 10^{16} \text{ ions/cm}^2$	9.11	7.27	75.0

emergence of nanoscale peaks and valleys, resulting in increased roughness parameters.

The AFM results revealed two predominant effects, namely (i) a reduction in the grain size within the nanostructured surface and (ii) an increase in the overall surface roughness. The grain size reduction can be attributed to ion-beam-induced dynamic recrystallization, which promotes morphological evolution and the formation of finer, more uniform grains. In contrast, the increase in surface roughness results from atomic redistributions and stress relaxation.

3.3. Optical properties

To investigate the optical properties of the studied materials, particularly to determine the energy bandgap of all ZnO thin film systems, UV-Vis spectrophotometry measurements were performed. Figure 3a presents the transmittance spectra, while Fig. 3b shows the reflectance as a function of photon energy, measured for ZnO thin films before and after ion implantation. As expected, a decrease in transmittance is observed in the ion-implanted samples. This reduction arises not only from the incorporation of C⁺ ions but also from the formation of a disordered defect layer on the ZnO surface, with a thickness approximately corresponding to the penetration depth of carbon ions. While at higher fluences this disordered layer is likely dominated by displacement-induced structural defects, even at the lowest implantation fluence ($\Phi = 10^{14} \text{ ions/cm}^2$), slight changes in the transmittance are observed, which may indicate ionization-induced modification of pre-existing native point defects, in particular oxygen vacancies (V_O). These vacancies are known to exist in multiple charge states, and trapping of carriers generated by electronic energy loss can lead to their recharging and activation as optically active centres [18, 23]. Similar effects have been observed previously in other oxide crystals implanted with carbon ions, where low-fluence ion irradiation led to changes in charge states and the creation of defect-related absorption bands [36]. These observations suggest that at low fluences, electronic energy loss may primarily result in carrier trapping at existing point defects or impurities rather than in the formation of new displacement-induced defects. The reflectance spectra (Fig. 3b) exhibit significant changes with increasing ion fluence, revealing progressive structural and optical modifications induced by implantation. In the case of the control ZnO thin film and ZnO implanted with lowest implantation fluence $(10^{14} ions/cm^2)$, a distinct absorption edge is clearly visible in the UV range, indicating the energy threshold at which ZnO begins to absorb light. However, as the fluence increases to $\Phi = 10^{15} \text{ ions/cm}^2$, the absorption edge becomes noticeably broadened and less defined, suggesting an increase in optical disorder and defectinduced band tailing effects. For the highest implantation fluence $\Phi = 10^{16} \text{ ions/cm}^2$, the spectra reveal a drastic increase in reflectance and a complete transformation of the optical response. AFM analysis shows that the ZnO layer remains morphologically continuous at the highest ion fluence $(\Phi = 10^{16} \text{ ions/cm}^2)$, therefore the drastic increase in reflectance observed in the UV-Vis spectra is unlikely to result from complete physical removal of the layer. Rather, they point toward extensive structural and electronic modification of the material, likely involving both displacement damage and cumulative ionization effects.

To restore the crystalline quality of the ZnO films, post-implantation annealing was carried out. In Fig. 3c-d, for clarity, we show data only for the sample implanted with the highest fluence $(\Phi = 10^{16} \text{ ions/cm}^2)$, where the effect of annealing was the strongest. Annealing leads to a substantial increase in transmittance (Fig. 3c) and a simultaneous reduction in reflectance (Fig. 3d), suggesting a partial recovery of optical transparency and a decrease in structural disorder. Notably, in the reflectance spectra (Fig. 3d), the characteristic absorption edge becomes sharper with increasing annealing temperature. AFM analysis revealed an increase in surface roughness after implantation. Therefore, the improved reflectance observed postannealing cannot be attributed to surface smoothing effects. Instead, the optical changes are more likely associated with the recrystallization of the ZnO structure and the reduction of defect states within the material. In this context, evaluating the optical bandgap (E_g) and the Urbach energy (E_U) provides valuable insight on the degree of structural disorder. The Urbach energy quantifies the exponential tail of sub-bandgap absorption, which is strongly influenced by disorder, lattice imperfections, and defect-induced states [37].

We calculated the bandgap energy (E_g) using the method proposed by Tauc [38]. The approach assumes that the energy-dependent absorption coefficient α follows the relationship

$$(\alpha h\nu)^{1/\gamma} = B (h\nu - E_g), \qquad (3)$$

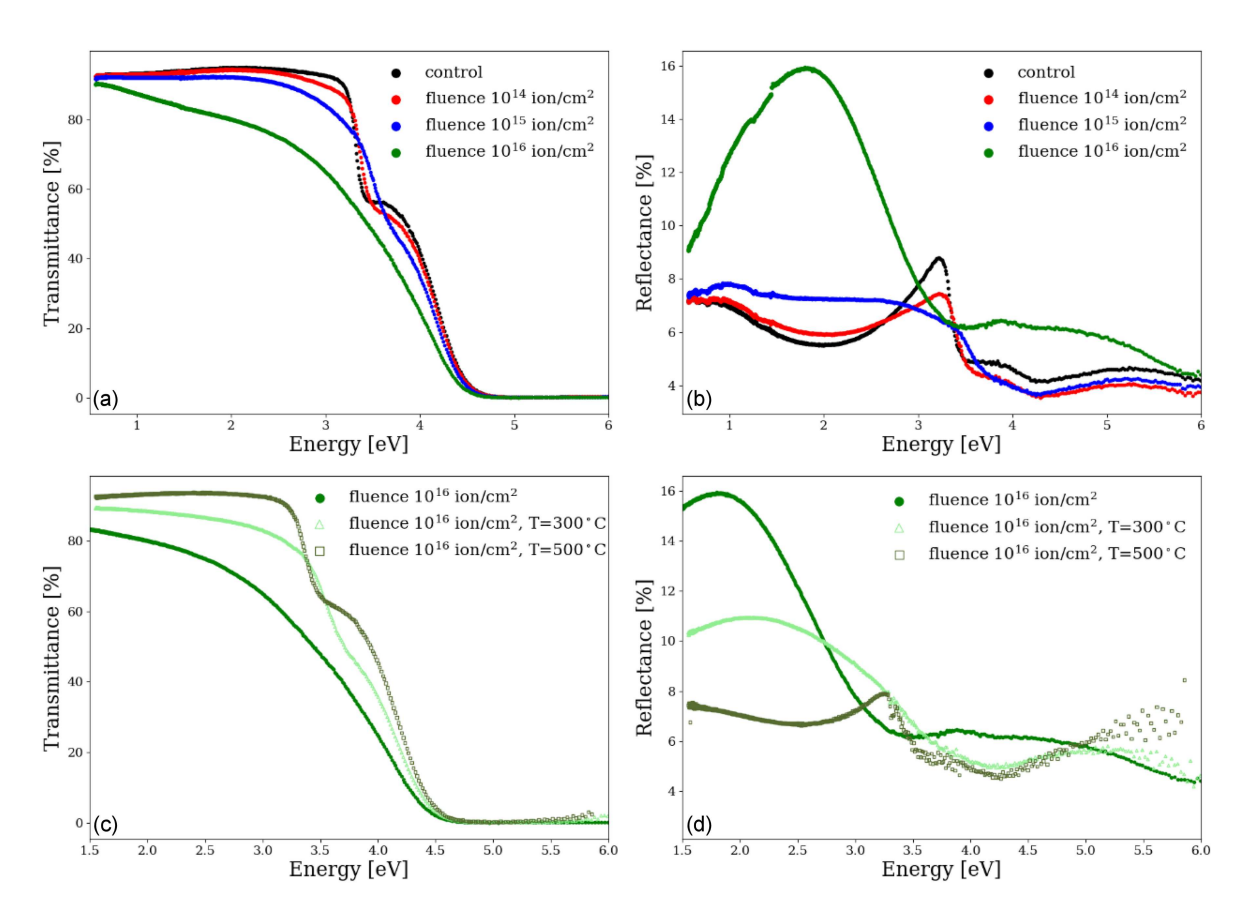


Fig. 3. UV-Vis transmittance (a, c) and reflectance (b, d) spectra of ZnO thin films. Panels (a) and (b) show the results before and after implantation with 20 keV C⁺ ions at different fluences (1 × 10¹⁴, 1 × 10¹⁵, 1 × 10¹⁶ ions/cm²). Panels (c) and (d) present the effect of post-implantation annealing at 300°C and 500°C on the sample implanted with $\Phi = 10^{16}$ ions/cm².

where h is Planck's constant, ν is the photon frequency, E_g is the energy of the bandgap, and B is a constant. The factor γ depends on the nature of the electronic transition and is equal to $\gamma=1/2$ for direct transitions, which occur in ZnO [39]. To estimate the bandgap energy, first the dependence described by (3) was determined and then a trend line was fitted to the linear section of the Tauc plot. The intersection of the trend line with the x-axis provides an estimate of the E_g value. The performed fittings are summarized in Fig. 4a, c, e, while the obtained results are presented in Table II.

As shown in Table II, the energy gap (E_g) for the control sample (prior implantation) is within the range of values reported in the literature, i.e., 3.27--3.33 eV [2]. In the case of ZnO implanted with fluences $\Phi=10^{14}$ ions/cm² and $\Phi=10^{15}$ ions/cm², E_g increases, which may indicate a shift of the valence band or conduction band edge. However, with a further increase in the fluence of implanted carbon ions ($\Phi=10^{16}$ ions/cm²), the $\alpha h \nu(E)$ dependence deviates from linearity. Table II also shows that annealing reduces E_g values, restoring them to near-control levels for $\Phi=10^{14}$ ions/cm² and $\Phi=10^{15}$ ions/cm², while for the highest fluence, E_g remains slightly higher at 3.33 eV.

TABLE II The E_g and E_U values for ZnO thin films implanted with 20 keV $\mathrm{C^+}$ ions with different ion fluences and post-annealed at 300°C and 500°C.

C ⁺ ion fluence	T [°C]	E_g [eV]	E_U [meV]
Control Φ	0	3.29	45.5
$arPhi_1=10^{14} \; \mathrm{ions/cm^2}$	0	3.31	102.8
	300	3.31	79.8
	500	3.29	49.7
	0	3.39	278.9
$\Phi_2 = 10^{15} \text{ ions/cm}^2$	300	3.38	155.8
	500	3.30	60.5
$arPhi_3=10^{16}~{ m ions/cm^2}$	0	_	751.1
	300	3.44	272.1
	500	3.33	72.2

To gain deeper insight into the structural disorder induced by carbon ion implantation, the absorption edge behavior was analyzed according to the Urbach formalism [40]. The characteristic exponential dependence of the absorption coefficient near the transparency edge reflects the presence of localized

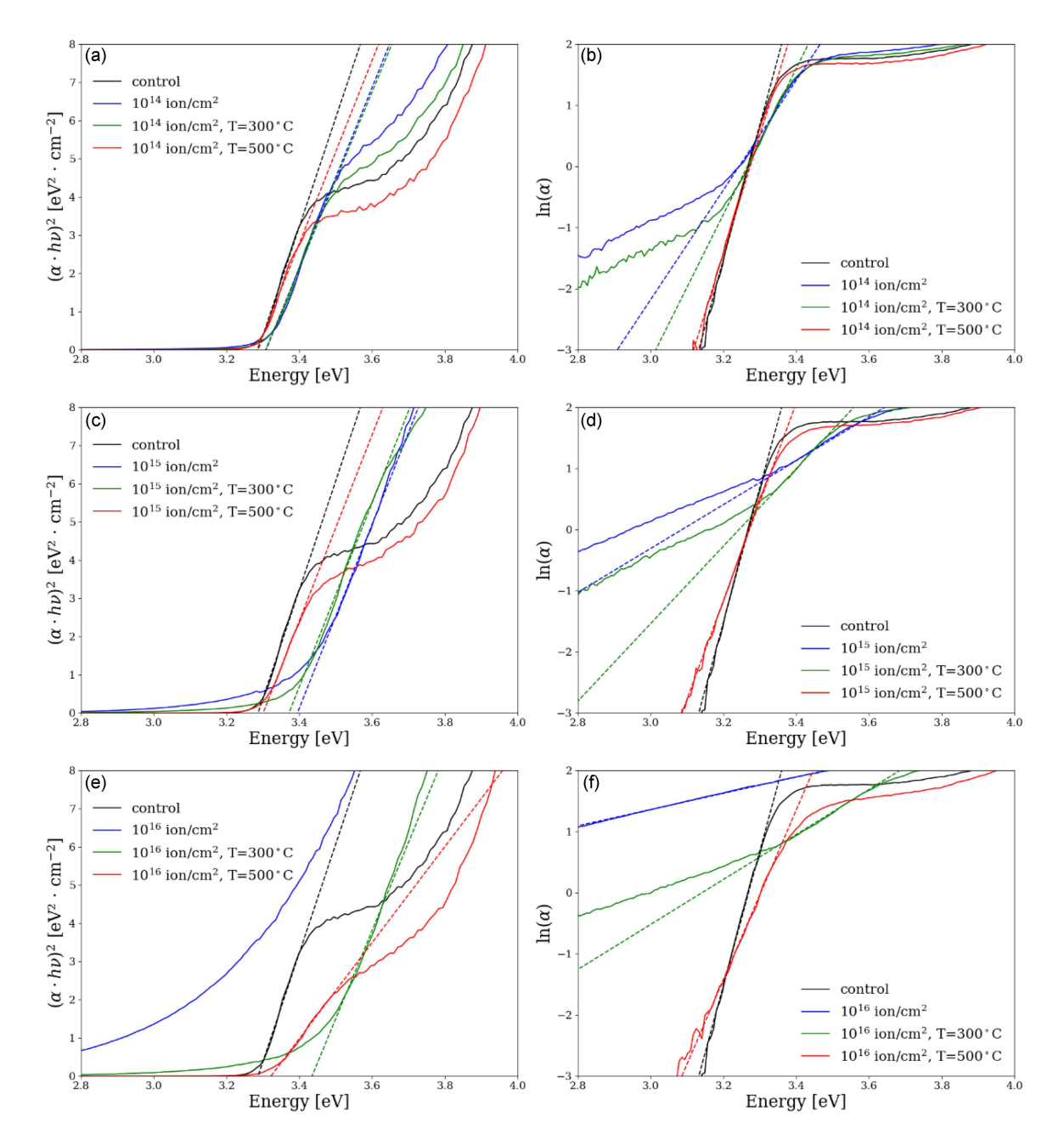


Fig. 4. UV-Vis optical analysis of ZnO thin films. Panels (a), (c), and (e) show the Tauc's plots for samples implanted with fluences of $\Phi=10^{14}~\rm ions/cm^2$, $\Phi=10^{15}~\rm ions/cm^2$, $\Phi=10^{16}~\rm ions/cm^2$, respectively. Each plot includes data for the as-deposited (control) sample, the as-implanted sample, and samples annealed at 300°C and 500°C. Panels (b), (d), and (f) present the corresponding Urbach plots.

states and structural disorder. This method provides valuable information on the electronic structure, phonon spectrum, and exciton—phonon coupling in the system [41, 42]. In crystalline semiconductors, the absorption edge is sharp, whereas in disordered or amorphous materials it becomes progressively broadened, leading to an increase in E_U . To determine E_U , we used Urbach rule, which describes the relationship between the absorption coefficient and the photon energy $h\nu$. Thus,

$$\alpha (E) = C e^{E/E_U}, \tag{4}$$

where α is the absorbance below the optical gap $(E < E_g)$, C is a constant, and E_U is a parameter referred to as the Urbach energy, which describes the extent of the distribution of the electronic band tail states. Taking the natural logarithm of both sides of (4) gives

$$\ln\left(\alpha\left(E\right)\right) = \frac{E}{E_{U}} + \ln(C). \tag{5}$$

Thus, E_U can be extracted from the inverse slope of a linear fit to the $\ln(\alpha(E))$ dependence in the low-energy region of the absorption spectrum.

Figure 4b, d, f presents the results of this analysis for ZnO thin films before and after carbon implantation. The obtained data clearly show that with increasing ion fluence, E_U systematically increases, which indicates an increasing density of localized states and enhanced structural disorder. This behavior is consistent with the progressive accumulation of damage of the ZnO lattice. Interestingly, post-implantation annealing leads to a partial reversal of this trend. The Urbach energy decreases after thermal treatment, approaching the values observed in the control sample. The calculated E_U values for each sample are summarized in Table II.

4. Conclusions

Our results demonstrate that carbon ion implantation induces morphological modifications in nanostructured ZnO thin films. Grains become smaller and exhibit a more anisotropic distribution, indicating implantation-driven fragmentation and surface reorganization. Importantly, despite exposure to energetic carbon ions, the ZnO film remains continuous, with no signs of surface cratering, delamination, or other macroscopic damage.

TRIM simulations indicate that carbon implantation in ZnO thin films generates a high density of lattice defects within the near-surface region of approximately 30–35 nm. Zn vacancies $(\rm V_{\rm Zn})$ are produced more efficiently than O vacancies $(\rm V_{\rm O})$, consistent with the lower displacement energy of Zn atoms. Vacancy profiles extend up to 100 nm, overlapping with the depth range of the implanted carbon.

Optical analysis shows that although the variation in the optical bandgap (E_g) is relatively small, especially at lower ion fluences, implantation significantly affects the sub-bandgap electronic structure. Increased Urbach energies and deviations from linearity in the Tauc plots at the highest fluence indicate increased structural disorder.

Post-implantation annealing reduce this disorder, as reflected by a decrease in the Urbach energy. However, the slightly increased E_g (3.33 eV) observed after annealing of ZnO thin films implanted with highest ions fluence can indicate the formation and stabilization of carbon-related defect complexes.

References

- M. Gartner, H. Stroescu, D. Mitrea, M. Nicolescu, Molecules 28, 4674 (2023).
- [2] J. Theerthagiri, S. Salla, R.A. Senthil et al., Nanotechnology 30, 392001 (2019).
- [3] F. Rahman, Opt. Eng. 58, 010901 (2019).

- [4] S.J. Pearton, F. Ren, Curr. Opin. Chem. Eng. 3, 51 (2014).
- [5] Y. Ning, Z. Zhang, F. Teng, X. Fang, Small 14, 1703754 (2018).
- [6] S.-J. Young, Y.-H. Liu, M.D.N.I. Shiblee et. al., ACS Appl. Electron. Mater. 2, 3522 (2020).
- [7] L. Zhu, L. Wang, F. Xue, L. Chen, J. Fu, X. Feng, T. Li, Z.L. Wang, Adv. Sci. 4, 1600185 (2016).
- [8] H. Yuan, S.A.A.A. Aljneibi, J. Yuan et. al., Adv. Mater. 31, 1807161 (2019).
- [9] W. Oum, A. Mirzaei, K.Y. Shin, E.B. Kim, S. Moon, S.S. Kim, H.W. Kim, Sens. Actuators B Chem. 435, 137615 (2025).
- [10] M. Boutamine, Y. Bakha, H. Saidani,
 H. Hachemi, A.D. Guerfi, C. Sabba,
 S. Aberkane, H. Khales, A. Bella, Acta
 Phys. Pol. A 145, 225 (2024).
- [11] I. Khan, A.A.M. Ibrahim, M. Sohail, A. Qurashi, *Ultrason. Sonochem.* **37**, 669 (2017).
- [12] V. Karpyna, Acta Phys. Pol. A 142, 644 (2022).
- [13] K.M. Lee, C.W. Lai, K.S. Ngai, J.C. Juan, Water Res. 88, 428 (2016).
- [14] V. Tiwari, N. Mishra, K. Gadani, P.S. Solanki, N.A. Shah, M. Tiwari, Front. Microbiol. 9, 1218 (2018).
- [15] S. Stankic, S. Suman, F. Haque, J. Vidic, J. Nanobiotechnol. 14, 73 (2016).
- [16] K. Rahmanifarah, M. Mahmoudian, S.M. Eskandarabadi, *Sci. Rep.* **15**, 3623 (2025).
- [17] I. Kim, K. Viswanathan, G. Kasi, S. Thanakkasaranee, K. Sadeghi, J. Seo, Food Rev. Int. 38, 537 (2022).
- [18] A. Das, D. Basak, ACS Appl. Electron. Mater. 3, 3693 (2021).
- [19] S.J. Pearton, D.P. Norton, K. Ip, Y.W. Heo, T. Steiner, J. Vac. Sci. Technol. B 22, 932 (2004).
- [20] S. Pal, A. Das, D. Basak, J. Appl. Phys. 135, 145105 (2024).
- [21] F. Kayaci, S. Vempati, I. Donmez, N. Biyikli, T. Uyar, *Nanoscale* 6, 10224 (2014).
- [22] J. Wang, R. Chen, L. Xiang, S. Komarnenic, *Ceram. Int.* 44, 7357 (2018).
- [23] J. Wang, Z. Wang, B. Huang, Y. Ma, Y. Liu, X. Qin, X. Zhang, Y. Dai, ACS Appl. Mater. Interfaces 4, 4024 (2012).
- [24] X. Bai, K. Luo, W. Cui, Z. Wang, Z. Ma, X. Wang, W. Zhang, X. Cui, *Vacuum* 221, 112940 (2024).

- [25] S.O. Kucheyev, J.S. Williams, C. Jagadish, J. Zou, C. Evans, A.J. Nelson, A.V. Hamza, *Phys. Rev. B* 67, 094115 (2003).
- [26] K. Lorenz, E. Alves, E. Wendler, O. Bilani, W. Wesch, M. Hayes, Appl. Phys. Lett. 87, 191904 (2005).
- [27] Z.Q. Chen, M. Maekawa, A. Kawasuso, S. Sakai, H. Naramoto, J. Appl. Phys. 99, 093507 (2006).
- [28] V. Sharma, M. Prasad, S. Jadkar, S. Pal, J. Mater. Sci. Mater. Electron. 27, 12318 (2016).
- [29] K. Saravanan, G. Jayalakshmi, S. Chandra et al., *Phys. Chem. Chem. Phys.* 19, 13316 (2017).
- [30] S. Zhou, Q. Xu, K. Potzger et. al., Appl. Phys. Lett. 93, 232507 (2008).
- [31] K. Wojtasik, M. Zięba, C. Tyszkiewicz, W. Pakieła, G. Żak, O. Jeremiasz, E. Gondek, K. Drabczyk, P. Karasiński, Materials 16, 1898 (2023).
- [32] B. Rajchel, M. Drwiega, E. Lipińska, M. Wierba, Nucl. Instrum. Methods Phys. Res. B 89, 342 (1994).
- [33] J.F. Ziegler, Srim The stopping and range of ions in matter (Ver. SRIM-2013).

- [34] D.C. Look, G.C. Farlow, P. Reunchan, S. Limpijumnong, S.B. Zhang, K. Nordlund, *Phys. Rev. Lett.* 95, 225502 (2005).
- [35] G.W. Egeland, J.A. Valdez, S.A. Maloy, K.J. McClellan, K.E. Sickafus, G.M. Bond, J. Nucl. Mater. 435, 77 (2013).
- [36] P. Potera, S. Ubizskii, D. Sugak, T. Lukasiewicz, *Radiat. Meas.* **42**, 232 (2007).
- [37] C. Kaiser, O.J. Sandberg, N. Zarrabi, W. Li, P. Meredith, A. Armin, *Nat. Commun.* 12, 3988 (2021).
- [38] P. Makuła, M. Pacia, W. Macyk, J. Phys. Chem. Lett. 9, 6814 (2018).
- [39] I.Y. Bouderbala, A. Guessoum, S. Rabhi,
 O. Bouhlassa, I.-E. Bouras, *Appl. Phys. A* 130, 205 (2024).
- [40] F. Urbach, *Phys. Rev.* **92**, 1324 (1953).
- [41] A.F. Zatsepin, Y.A. Kuznetsova, V.I. Sokolov, J. Lumin. 183, 135 (2017).
- [42] I.A. Vainshtein, A.F. Zatsepin, V.S. Kortov, Y.V. Shchapova, *Phys. Solid State* 42, 230 (2000).